HHS Public Access

Author manuscript

Neuroimage. Author manuscript; available in PMC 2015 April 22.

Published in final edited form as:

Neuroimage. 2015 March ; 108: 111–122. doi:10.1016/j.neuroimage.2014.12.043.

A method for estimating and removing streaking artifacts in quantitative susceptibility mapping

Wei Li[a,b,c,*], **Nian Wang**[a], **Fang Yu**[d], **Hui Han**[a], **Wei Cao**[a,e], **Rebecca Romero**[f], **Bundhit Tantiwongkosi**[d], **Timothy Q. Duong**[b], and **Chunlei Liu**[a,g,**]

Wei Li: liw5@uthscsa.edu; Chunlei Liu: Chunlei.liu@duke.edu

[a]Brain Imaging and Analysis Center, Duke University, Durham NC 27705, USA

[b]Research Imaging Institute, University of Texas Health Science Center at San Antonio, TX 78229, USA

[c]Department of Ophthalmology, University of Texas Health Science Center at San Antonio, TX 78229, USA

[d]Department of Radiology, University of Texas Health Science Center at San Antonio, TX 78229, USA

[e]Tongji Hospital, Tongji Medical College, Huazhong University of Science and Technology, Wuhan, Hubei 430030, China

[f]Department of Neurology, University of Texas Health Science Center at San Antonio, TX 78229, USA

[g]Department of Radiology, School of Medicine, Duke University, Durham NC 27705, USA

Abstract

Quantitative susceptibility mapping (QSM) is a novel MRI method for quantifying tissue magnetic property. In the brain, it reflects the molecular composition and microstructure of the local tissue. However, susceptibility maps reconstructed from single-orientation data still suffer from streaking artifacts which obscure structural details and small lesions. We propose and have developed a general method for estimating streaking artifacts and subtracting them from susceptibility maps. Specifically, this method uses a sparse linear equation and least-squares (LSQR)-algorithm-based method to derive an initial estimation of magnetic susceptibility, a fast quantitative susceptibility mapping method to estimate the susceptibility boundaries, and an iterative approach to estimate the susceptibility artifact from ill-conditioned k-space regions only. With a fixed set of parameters for the initial susceptibility estimation and subsequent streaking artifact estimation and removal, the method provides an unbiased estimate of tissue susceptibility with negligible streaking artifacts, as compared to multi-orientation QSM reconstruction. This method allows for improved delineation of white matter lesions in patients with multiple sclerosis and small structures of the

*Correspondence to: W. Li, Research Imaging Institute, University of Texas Health Science Center at San Antonio, 8403 Floyd Curl Drive, San Antonio, TX 78229, USA. **Correspondence to: C. Liu, Brain Imaging and Analysis Center, Duke University School of Medicine, 2424 Erwin Road, Suite 501, Durham, NC 27705, USA.

human brain with excellent anatomical details. The proposed methodology can be extended to other existing QSM algorithms.

Keywords

Quantitative susceptibility mapping; Streaking artifact removal; Multiple sclerosis; High resolution brain imaging

Introduction

The signal phase of gradient echo MRI provides much higher gray–white matter contrast than the corresponding magnitude, and contains unique information regarding deoxyhemoglobin, iron, myelin, and tissue microstructure (Duyn et al., 2007; He and Yablonskiy, 2009; Rauscher et al., 2005). Despite these promises, one intrinsic limitation is that phase value at one location depends on both the adjacent magnetic susceptibility distribution and the orientation with respect to the main magnetic field, and thus not suitable for quantitative assessment of tissues. Over the past few years, there have been growing efforts in developing quantitative susceptibility mapping (QSM), a novel MRI technology for solving the ill-posed phase-susceptibility equation to derive the voxel-wise magnetic susceptibility (de Rochefort et al., 2010; Kressler et al., 2010; Li et al., 2011; Liu et al., 2009, 2011b; Schweser et al., 2011b; Shmueli et al., 2009; Wharton et al., 2010; Wu et al., 2012). To date, QSM has been applied in studying cerebral micro-bleeds (Liu et al., 2012b), differentiating iron deposits from calcifications (Deistung et al., 2013), quantifying iron overload in Parkinson's diseases (Lotfipour et al., 2012), assessing the abnormalities in white matter myelination (Liu et al., 2011a), and in many other applications (Duyn, 2013; Reichenbach, 2012).

QSM attempts to solve an ill-posed inverse problem, and many methods have been developed to stabilize the inversion. While threshold-based k-space division or multi-orientation methods have been used in earlier studies (Liu et al., 2009; Shmueli et al., 2009), iterative solutions with regularization and prior information from magnitude or phase are increasingly used for single-orientation reconstruction with reduced streaking artifacts (de Rochefort et al., 2010; Liu et al., 2011b). Although prior information is highly useful in suppressing streaking artifacts around strong susceptibility sources, e.g. cerebral hematoma or large veins, one general concern is that excessive external constraints may alter the spatial frequencies of magnetic susceptibility in an unpredictable manner with degradation of tissue contrast. This is especially problematic for evaluating white matter lesions, whose susceptibility variations are small compared to that of major brain gray and white matter structures. Similar concerns also exist for studying small gray matter structures in the human brain, e.g. subthalamic nucleus, substantia nigra, cerebellar nuclei, which are small in size but have vital functions. Hence, eliminating streaking artifacts while minimizing the regularization-related confounding factors is crucial for evaluating subtle contrast changes in white matter diseases and for delineation of small but functionally important brain structures.

Previously, several methods have been proposed to separate the k-space into different sub-regions and to apply constraints only on ill-posed and ill-conditioned sub-regions (Li et al., 2011; Schweser et al., 2012; Wu et al., 2012). The results suggest that optimization of the ill-conditioned k-space region alone can reduce streaking artifacts. In this study, we propose a general method for estimating streaking artifacts and subtracting them from susceptibility maps. We demonstrate the application of the methodology in reducing streaking artifacts for the LSQR algorithm (Li et al., 2011). We show that, by estimating and subtracting out the streaking artifacts, reproducible QSM can be achieved with negligible streaking artifacts. This method allows for improved delineation of white matter lesions in multiple sclerosis patients and small brain structures in healthy human brains that otherwise would have been obscured by streaking artifacts. The proposed methodology can be extended to other existing QSM algorithms.

Materials and methods

A method for estimating streaking artifacts

The normalized phase ($\psi = \phi/\gamma\mu_0 H_0 TE$) and magnetic susceptibility (χ) can be related using the following equation (Koch et al., 2006; Marques and Bowtell, 2005; Salomir et al., 2003):

$$\psi = FT^{-1}\{D_2 \cdot FT(\chi)\} \quad (1)$$

where γ, μ_0, H_0, and TE, are the gyromagnetic ratio, vacuum permeability, applied magnetic field, and echo time, respectively; FT means Fourier transform; and D_2 can be calculated from the spatial frequency ($\mathbf{k}$) and the field direction $\hat{\mathbf{H}}$ as:

$$D_2 = \frac{1}{3} - \left(\hat{\mathbf{H}} \cdot \mathbf{k}\right)^2 \left(k_x^2 + k_y^2 + k_z^2\right)^{-1}. \quad (2)$$

For a given initial susceptibility estimation (χ_0) obtained by solving Eq. (1), the streaking artifacts can be assumed to have originated from inaccuracies of inversion at ill-conditioned k-space regions. As such, the susceptibility artifacts in the k-space, $\chi_{SA}(k)$, can be estimated using the following minimization using the LSQR solver in Matlab:

$$\min_{\chi_{SA}(k)} \sum_i \| W_{Gi} \cdot G_i \left\{ \chi_0 - FT^{-1}[\chi_{SA}(k) \cdot M_{IC}] \right\} \|_2 \quad (3)$$

where $i = x, y$ and z; G_i are gradient operators; W_{Gi} are corresponding weights, which can be determined according to the estimated susceptibility boundaries and are defined in later sections; M_{IC} is a binary mask of the ill-conditioned k-space regions:

$$M_{IC} = |D_2(k)| < D_{2,thres} \quad (4)$$

where $D_{2,\text{thres}}$ is the threshold for M_{IC} calculation.

The final susceptibility is obtained by subtracting the susceptibility artifacts from the initial susceptibility estimated by the LSQR method (χ_{LSQR}):

$$\chi_{iLSQR}=\chi_{LSQR}-FT^{-1}\left[\chi_{SA}(k)\cdot M_{IC}\right]. \quad (5)$$

For simplicity, the full method is referred to as the “iLSQR” method.

Initial susceptibility estimation using LSQR

The LSQR method has been described previously (Li et al., 2011), which solves the following equation:

$$FT^{-1}\left\{D_2\cdot FT(W_I\cdot\psi)\right\}=FT^{-1}\left\{D_2\cdot FT\left[W_I\cdot FT^{-1}\left\{D_2\cdot FT\left(\chi_{LSQR}\right)\right\}\right]\right\}. \quad (6)$$

In this study, an image-space weighting term (W_I) is added to reduce artifacts arising from the inaccurate phase unwrapping around strong magnetic susceptibility sources. In this equation, the ill-conditioned phase-susceptibility relationship is weighted by another D_2 term in k-space for preconditioning. Since tissue interfaces with sharp phase changes are more prone to errors, W_I is determined using the Laplacian of the phase data ($\nabla^2\phi$) as:

$$\begin{cases} W_I=1,\ \nabla^2\varphi<\nabla^2\varphi_{\min} \\ W_I=\left(\nabla^2\varphi_{\max}-\nabla^2\varphi\right)/\left(\nabla^2\varphi_{\max}-\nabla^2\varphi_{\min}\right),\ \nabla^2\varphi_{\min}\le\nabla^2\varphi\le\nabla^2\varphi_{\max} \\ W_I=0,\ \nabla^2\varphi_{\max}<\nabla^2\varphi. \end{cases} \quad (7)$$

Here $\nabla^2\phi_{\min}$ and $\nabla^2\phi_{\max}$ are the thresholds used for calculating W_I, which can be adjusted to deal with different levels of phase unwrapping errors. Eq. (6) can be solved iteratively using the LSQR (Paige and Saunders, 1982) solver in Matlab. This LSQR allows for fast reconstruction of magnetic susceptibility with reasonable suppression of streaking artifacts, and provides an excellent initial estimation of susceptibility.

Susceptibility boundary estimation with fast QSM

Streaking artifact estimation requires an estimation of the susceptibility boundaries for determining the weighting terms. Previously, Wharton and Bowtell (2010) showed that inaccurate boundary constraints will lead to distorted structures in the final susceptibility maps (Wharton and Bowtell, 2010). It is well known that the boundaries of magnitude and phase do not necessarily match that of susceptibility. As a result, they will lead to inaccurate susceptibility maps if used to generate the weighting masks. To address this problem, we developed a method for fast estimation of susceptibility contrast (referred to as the “fast QSM” method) with minimal streaking artifacts. This method provides a more accurate contrast for generating the weighting masks (W_{Gi}) compared to magnitude and phase.

The first step of this fast QSM method is to calculate an estimate of susceptibility contrast (in k-space) based on the positive or negative sign of D_2:

$$\chi_{F1}(k)=sign(D_2)\cdot FT(\psi). \quad (8)$$

A discontinuity in $\chi_{F1}(k)$ across the conical surface (defined by $D_2 = 0$) is expected, which is a significant source of streaking artifacts after Fourier transform. To attenuate this discontinuity, the discontinuous k-space data is averaged along the conical surfaces and inverse Fourier transformed into the image space:

$$\chi_{F2}=FT^{-1}\left\{\chi_{F1}(k)\cdot W_{FS}+Filter[\chi_{F1}(k)]\cdot(1-W_{FS})\right\} \quad (9)$$

where *Filter* represents a low-pass filtering operation to remove the discontinuity. In this study, a spherical mean value filter is used with a small radius of 2–3 mm to ensure the locality of the k-space data, and W_{FS} is an empirically determined continuous function of D_2 so that the "averaging" of k-space data is restricted to ill-conditioned regions:

$$W_0=\left(|D_2|^{0.001}-a\right)/(b-a)\begin{cases} W_{FS}=0,\ W_0<0 \\ W_{FS}=W_0,\ 0<W_0<1 \\ W_{FS}=1,\ 1<W_0. \end{cases} \quad (10)$$

Here *a* and *b* are the 1st and 30th percentile values of $|D2|^{0.001}$, respectively.

The resulting χ_{F2} still contains streaking artifacts, which is obvious in the regions outside the brain. The streaking artifacts outside the brain can be removed through masking. The masked χ_{F2} is Fourier transformed into frequency domain, to spread the masking effect into different frequency components. Another k-space "averaging" is repeated to further reduce the streaking artifacts, followed by an inverse transform back into the image space and masking:

$$\chi_{F3}=FT^{-1}\left\{FT(Mask\cdot\chi_{F2})\cdot W_{FS}+Filter[FT(Mask\cdot\chi_{F2})]\cdot(1-W_{FS})\right\}\cdot Mask \quad [11]$$

where Mask represents the binary mask for the tissue of interest. The resulting susceptibility estimates (χ_{F3}) provide the same boundaries as the quantitative susceptibility with negligible artifacts. The limitation is that χ_{F3} underestimate the tissue susceptibility.

To correct for this underestimation, a thresholded k-space division reconstruction of magnetic susceptibility is performed to derive a quantitative map with streaking artifacts, but having the correct scale of susceptibility contrast (χ_{TKD}) (Shmueli et al., 2009):

$$\begin{cases} D_{2,TKD}=D_2,\ |D_2|\geq t_0 \\ D_{2,TKD}=t_0,\ 0\leq D_2<t_0 \\ D_{2,TKD}=-t_0,\ -t_0<D_2<0 \end{cases} \quad (12)$$
$$\chi_{TKD}=Mask\cdot FT^{-1}\left[\left(D_{2,TKD}\right)^{-1}FT(\psi)\right]$$

where the threshold t_0 was set to 1/8. The resulting χ_{TKD} is used to determine the linear scaling factor (*a*) and baseline difference (*b*) between χ_{F3} and χ_{TKD} through the following minimization:

$$\min_{a,b}\|a\cdot\chi_{F3}+b-\chi_{TKD}\|_2. \quad (13)$$

The final susceptibility estimate by fast QSM (χ_{FS}) is then derived as:

$$\chi_{FS}=a\cdot\chi_{F3}+b. \quad (14)$$

The weights in Eq. (3) can be determined from χ_{FS} as follows:

$$\begin{cases} W_{Gi}=1,\ G_i(\chi_{FS})<G_{i,\min} \\ W_{Gi}=[G_{i,\max}-G_i(\chi_{FS})]\,/\,[G_{i,\max}-G_{i,\min}],\ G_{i,\min}<G_i(\chi_{FS})<G_{i,\max} \\ W_{Gi}=0,\ G_{i,\max}<G_i(\chi_{FS}) \end{cases} \quad [15]$$

where $i = x, y$ or z. $G_{i,\max}$ and $G_{i,\min}$ are the thresholds for gradient weight calculation.

Human brain MRI

In vivo brain imaging of a 33-year-old healthy volunteer was scanned at the Brain Imaging and Analysis Center at Duke University using a GE MR750 3.0 T scanner (GE Healthcare, Waukesha, WI) equipped with an 8-channel head coil. The images were acquired using a non-flow-compensated multi-echo spoiled-gradient-recalled (SPGR) sequence with bipolar echo readout gradients, and the following parameters: TE1 = 5 ms, echo spacing = 4.86 ms, number of echoes = 16, TR = 80 ms, flip angle = 20°, FOV = 192 × 192 mm^2, matrix size = 320 × 320, slice thickness = 0.6 mm, 200 slices, total imaging acquisition time = 85 min. This protocol resulted in 0.6 mm isotropic resolution. The same scans were repeated with two different head orientations with respect to the B0 field. The $\hat{\mathbf{H}}$ vectors for the three acquisitions referenced to the first acquisition were: (0, 0, 1), (−0.263, 0.015, 0.965) and (0.103, 0.400, 0.911), which correspond to (0°, 0°), (−15.2°, 0.8°) and (5.9°, 23.9°) rotations about the y- and x-axes, respectively. Another set of high resolution phase images covering the whole cerebellum and brain stem was acquired on the same subject with the following parameters: TE1 = 5 ms, echo spacing = 3.49 ms, number of echoes = 16, TR = 70 ms, flip angle = 20°, FOV = 160 × 160 mm^2, matrix size = 320 × 320, slice thickness = 0.5 mm, 184 slices, total imaging time = 69 min. This set of imaging parameters yielded a 0.5 mm isotropic spatial resolution.

In vivo brain imaging of 10 adult participants with 1 × 1 × 1 mm^3 spatial resolution was also acquired in a standard flow-compensated 3D SPGR sequence with the following parameters: TE = 23 ms; TR = 30 ms; flip angle, 20°; FOV, 256 × 256 mm^2; matrix size, 256 × 256; slice thickness = 1 mm, 120 slices; SENSE factor, 2. All of the above experiments were approved by the institutional review board of Duke University.

In vivo brain imaging of 6 patients with multiple sclerosis (MS) were acquired on a Philips Achieva 3 T scanner using the 3D mFFE sequence (a multiple-echo gradient echo sequence for Philips scanners) with the following parameters: flip angle, 20°; TE1 = 4.20 ms; echo spacing = 4.80 ms; TR = 36.56 ms; FOV = 230 × 230 mm^2; matrix size = 256 × 256; slice thickness = 2 mm; SENSE factor, 2. This set of imaging parameters yielded a 0.9 × 0.9 × 2 mm^3 anisotropic voxel size. To obtain the mask for cortical white matter, T1-weighted images were acquired in 4 patients with a T1-TFE sequence with the following parameters: FOV = 256 × 256 mm^2; matrix size = 256 × 256; flip angle 8°; TE = 4.6 ms; TR = 9.89 ms

and 180 slices, slice thickness = 1 mm. All experiments were approved by the institutional review board of the University of Texas Health Science Center at San Antonio.

Phase and susceptibility reconstruction

To achieve optimal image quality, the data from different coils were combined from the raw k-space data for high resolution (0.5 or 0.6 mm isotropic) brain images. Briefly, the brain images from each receiver coil were reconstructed with 3D Fast Fourier transform. Since coil phase differences between different coils are smooth and not vary with echo time, the coil phase differences ($\Delta\phi$) were obtained from the phase of the first echoes as:

$$\Delta\varphi_{c,1}=Filter\ (\varphi_{c,1}-\varphi_{ref,1}) \quad [16]$$

where the low pass filtering (*Filter*) used the spherical mean value (SMV) filter with a radius of 5 mm. The subscript *c* represents the coil number, and coil *ref* represents the reference coil. The coil with the most homogeneous intensity throughout the field of view was selected as the reference. The second subscript represents the echo number, and is 1, since the first echo is used. The coil-phase-corrected phase ($\phi_{c,e} - \Delta\phi_{c,1}$) and the magnitude of the complex signal $|S_{c,e}|$ were recombined and summed to derive the final complex signal (S_e) for echo *e* as follows:

$$S_e=\sum_{c=1}^{nc}\{|S_{c,e}|\cdot\exp\ [i\cdot(\varphi_{c,e}-\Delta\varphi_{c,1})]\} \quad (17)$$

where *nc* is the number of coils. The final complex signal was then separated into magnitude and phase for each echo. For all other datasets, the default methods provided by the scanner were used to combine the data from different coils.

The magnitudes of high-resolution brain images were used for semi-automatic brain extraction using ITK-SNAP (http://www.itksnap.org), which offer more control over the details of tissue extraction for optimal high resolution QSM. For the other datasets, automatic brain extraction employed the BET tool provided by FSL (FMRIB, Oxford University, UK). The phase from the 16 echoes was unwrapped using Laplacian-based unwrapping (Li et al., 2011). The normalized phase ψ was then calculated as:

$$\psi=\sum_{e=1}^{ne}\varphi_e/\gamma\mu_0 H_0\sum_{e=1}^{ne}TE_e. \quad (18)$$

The normalized background phase was removed using the V-SHARP method with the spherical mean radius increasing from 0.6 mm at the boundary of the brain to 25 mm towards the center of the brain (Li et al., 2014a; Wu et al., 2012). χ_{LSQR} was calculated from the normalized background removed phase using the Matlab LSQR solver (Eq. (6)). The streaking artifacts χ_{SA} were then estimated subsequently using the LSQR methods (Eq. (3)). The final susceptibility maps (χ_{iLSQR}) were obtained as $\chi_{LSQR} - \chi_{SA}$ (Eq. (5)). Using the three-orientation dataset, the susceptibility were also reconstructed using the COSMOS method (Liu et al., 2009). Similar to the previous study (Li et al., 2014b), susceptibility values obtained by various QSM methods were directly used for comparisons, which essentially sets the susceptibility reference to the mean susceptibility of the whole brain.

Parameter optimization and analysis

The parameter optimization of the iLSQR method was focused on the error tolerances for the initial LSQR calculation, and the D_2 thresholds for streaking artifact removal with the aim of obtaining an unbiased quantification of magnetic susceptibility. As shown in the Results section, the overall susceptibility contrast in the initial susceptibility estimation by LSQR increases with decreasing error tolerance compared to COSMOS. A fixed error tolerance of 0.02 provides an unbiased quantification of magnetic susceptibility. For streaking artifact estimation, a fixed $D_{2,\text{thres}}$ of 0.1 provides effective removal of streaking artifacts. However, the subtraction of streaking artifacts also lowers the overall susceptibility contrast. To compensate this effect of lowering susceptibility contrast, an error tolerance of 0.01 instead of 0.02 in the initial LSQR estimation is chosen that results in slightly higher initial susceptibility contrast. With the combination of an error tolerance of 0.01 for initial LSQR estimation and a $D_{2,\text{thres}}$ of 0.1 for streaking artifact removal, the iLSQR method provides unbiased susceptibility contrast as compared to COSMOS.

To evaluate the validity of the selected parameters, iLSQR was compared to COSMOS with different in-plane resolutions (i.e. 0.8 × 0.8, 0.9 × 0.9 and 1.0 × 1.0 mm^2) and different slice thicknesses (from 0.8 to 4 mm) for the 33-year-old healthy volunteer. A trilinear interpolation was applied to the final background removed phase and the COSMOS-determined susceptibility to obtain phase and the reference susceptibility data with the targeted spatial resolution. To further evaluate the inter-subject variability, we compared the iLSQR and LSQR (with the error tolerance of 0.02 for unbiased susceptibility quantification) on the 10 adult participants with 1 × 1 × 1 mm^3 spatial resolution. This comparison used a region of interest (ROI)-based approach. The ROIs were drawn using the tools provided in STI Suite (Li et al., 2014a), which includes globus pallidus (GP), putamen (PU), caudate nucleus (CN), red nucleus (RN), substantia nigra (SN), dentate nucleus (DN), splenium of corpus callosum (SCC) and internal capsule (IC).

For the image analysis of the MS patients, the ROIs were drawn on the white matter lesions and the surrounding normal appearing white matter using STI Suite (n = 6). A total of 22 lesions were measured from these 6 patients, with each patient contributing 3 to 4 white matter lesions. Since the visualization of white matter lesions is also influenced by the homogeneity of surrounding tissues, the white matter segmentation was performed using T1-weighted images with the FAST tool provided by FSL (FMRIB, Oxford University, UK) based on the registered T1 maps, and the susceptibility variation of the cortical white matter was determined as the standard derivation (n = 4).

All the programs were written using Matlab R2011b (Mathworks, Natick, MA), which is provided in “STI Suite” version 2.0 (http://people.duke.edu/~cl160). The calculations were performed on a Dell XPS8700 desktop computer with an Intel Core i7-4790™ processer and 12GB RAM.

Results

Overview of the iLSQR method

Fig. 1 illustrates the algorithmic steps of the proposed streaking artifact removal method. The three inputs for streaking artifact estimation are the initial susceptibility estimate χ_{LSQR} (Fig. 1A), the binary mask of the ill-conditioned k-space regions M_{IC} (Fig. 1B) and the weighting functions W_{Gi} (Fig. 1D). Here, the weighting functions W_{Gi} are determined using the susceptibility map by the fast QSM method (Fig. 1C). The susceptibility artifacts χ_{SA} (Fig. 1E) are then calculated by solving Eq. (3). The final susceptibility map was obtained by subtracting the susceptibility artifacts from the initial susceptibility estimate (Fig. 1F).

Fast QSM for estimating susceptibility boundaries

Fig. 2 shows the procedure of fast QSM method. Fig. 2A and B shows the phase obtained using the V-SHARP method and the corresponding W_{FS} values. With a single step of inversion (Fig. 2D), and the corresponding susceptibility estimates contains a small amount of streaking artifacts (Fig. 2C). With the further conical k-space averaging and scaling (Fig. 2F), the resulting susceptibility map contains minimal streaking artifacts (Fig. 2E). The computation time is 8 and 12 s for representative matrix sizes of 256 × 256 × 256 and 320 × 320 × 320, respectively.

Initial susceptibility estimation using LSQR

The initial susceptibility estimation was performed by LSQR using background removed phase and weights (W_I) obtained from Laplacian of the phase (Fig. 3A) with different error tolerances (Figs. 3B–D). For W_I calculation, the values of $\nabla^2\phi_{\min}$ and $\nabla^2\phi_{\max}$ were empirically set to the 60th and 99.9th percentile values of $\nabla^2\phi$, respectively. As a result, 0.1% of voxels within the brain mask have weight of 0, and 1.2% of voxels have weight in the range of 0 to 0.5, and the rest 98.7% of voxels have weight from 0.5 to 1. In our extensive testing, these choices have generally performed robustly. The amount of streaking artifacts increases with decreasing error tolerance (or increasing iterations steps). There is negligible amount of streaking artifacts using a tolerance of 0.05, while there is a significant amount of artifacts for a tolerance of 0.005.

iLSQR and parameter optimization

For the initial estimation of susceptibility with LSQR method, along with the changing amount of streaking artifacts, the susceptibility contrast is also changing with the error tolerance. To evaluate dependence of susceptibility contrast on the error tolerance, we correlated the χ_{LSQR} with the susceptibility determined by COSMOS (Fig. 3E). The linear correlation used a total least square (TLS) method (Fig. 3F), which provides quantitative information regarding the degree of underestimation (slope < 1) or overestimation (slope > 1) with respect to COSMOS. From Fig. 3G, with the error tolerance decreasing from 0.1 to ~0.02, the LSQR-determined susceptibility is changed from significant underestimation towards an unbiased estimate of susceptibility. The unbiased estimation is achieved with an error tolerance of ~0.02. With further decrease of error tolerance from 0.02 to 0.002, the LSQR-determined susceptibility is increasingly overestimated. This slope was slightly

affected by the spatial resolution. For a tolerance of 0.02, the slopes are 0.98, 1.06 and 1.10 for the voxel sizes of 0.6 × 0.6 × 0.6 mm^3, 1 × 1 × 1 mm^3 and 0.9 × 0.9 × 2 mm^3, respectively.

For the streaking artifact removal, the D_2 threshold determines both the efficacy of streaking artifact removal and the slope with respect to COSMOS (Fig. 4). A small $D_{2,thres}$ of 0.02 is not enough for removing all streaking artifacts, a $D_{2,thres}$ of 0.1 is able to reproducibly eliminate the majority of streaking artifacts, and the obtained streaking artifacts do not contain anatomical structures. The estimated susceptibility artifacts with a large $D_{2,thres}$ of 0.18 will contain anatomical structures (Fig. 4C). These observations hold for other spatial resolution studied. A quantitative assessment of streaking artifacts is provided in the Supplementary material. Importantly, the slope of the final susceptibility with respect to that by COSMOS decreases with larger D_2 threshold used for streaking artifact estimation (Fig. 4J). In the above calculations, $G_{i,min}$ and $G_{i,max}$ were empirically set to the 50th and 70th percentile values of $G_i(\chi_{FS})$ for the determination of W_{Gi}.

Considering the opposite trend shown in Figs. 3G and 4J, we fixed an error tolerance of 0.01 for the initial LSQR method and a $D_{2,thres}$ of 0.1 for streaking artifact estimation. To evaluate the validity of this set of parameters, three typical in-plane resolutions of 0.8 × 0.8 mm^2, 0.9 × 0.9 mm^2 and 1.0 × 1.0 mm^2 were evaluated using the iLSQR method with slice thickness ranging from 0.8 to 4 mm (Fig. 4K). For these typical in-plane resolutions, the slope was within the range of 0.98–1.03 for all the slice thicknesses from 0.8 to 2.5 mm, and was within the range of 0.94–1.06 for the slice thicknesses of 3 mm and 4 mm.

To evaluate the inter-subject variability, we compared LSQR (with an error tolerance of 0.02) and the iLSQR method for adult participants (n = 10) with a spatial resolution of 1 × 1 × 1 mm^3 (Figs. 5A and B). The calculated susceptibility maps using the iLSQR method do not contain apparent streaking artifacts. The difference image between LSQR and iLSQR are mainly streaking artifacts (Fig. 5D). Consistent with previous results, the susceptibility of these main brain structures agrees with each other very well with a correlation coefficient of 1.001 and R^2 of 0.997 (Fig. 5F). For this dataset, the computation time of the LSQR, and iLSQR method for each dataset was 50.4 ± 3.6 s, and 180 ± 13 s, respectively (not including phase unwrapping and background phase removal).

In the same Fig. 5, comparison was also performed between iLSQR and fast QSM, since fast QSM could potentially be useful as a fast approximation of susceptibility contrast. As was shown in Fig. 5C, the fast QSM showed slightly less streaking artifacts than the iLSQR method. The contrast by fast QSM is very similar to that by iLSQR, however the difference image revealed some anatomical structures (white arrow). Nevertheless, susceptibilities by fast QSM and iLSQR showed good linearity with a slope of 1.038, and R^2 of 0.967 (Fig. 5G). In terms of computation time, fast QSM took significantly shorter time (9.7 ± 0.3 s) than iLSQR (180 ± 13 s).

Comparison of different QSM methods for delineation of MS lesions

The LSQR, iLSQR and fast QSM methods were applied to the MS patients (n = 6). The representative susceptibility maps by LSQR and iLSQR (with an error tolerance of 0.02)

were shown in the left two columns of Fig. 6. The iLSQR-determined susceptibility showed a trend of lower variations across cortical white matter than LSQR (iLSQR: 0.019 ± 0.003 ppm, LSQR: 0.023 ± 0.002 ppm, $P > 0.05$, $n = 4$). Accordingly, iLSQR provided slightly better visualization of white matter lesions than LSQR. The fast-QSM-determined susceptibility provides the lowest variations across cortical white matter (0.017 ± 0.002 ppm), and similar visualization of white matter lesions as iLSQR. Quantitatively, the three methods provide similar susceptibility contrast between MS lesion and surrounding white matter tissues (LSQR: 0.037 ± 0.012; iLSQR: 0.034 ± 0.009 ppm; fast QSM: 0.030 ± 0.008 ppm, $P > 0.05$, $n = 22$ lesions from 6 subjects). The susceptibility by LSQR and fast QSM are both linearly correlated with iLSQR (Fig. 6J), although the slopes are deviated from 1 (LSQR: 1.116 and fast QSM: 0.825).

iLSQR provides excellent anatomical details of small brain structures

With demonstrated better image quality, the iLSQR was directly applied for high resolution QSM without further comparison with the LSQR method. Fig. 7 shows the cerebellar nuclei at 0.5 mm isotropic resolution. The cerebellar nuclei are comprised of several sub-structures, i.e. dentate nucleus, globose nucleus, fastigial nucleus, and emboliform nucleus. All of these gray matter nuclei contain high iron content. In addition, the dentate nucleus is also highly folded. From the figure, magnitude contrast is not sharp due to blooming artifacts, while the phase contrast shows strong non-local effects. In contrast, the susceptibility by the fast QSM method provided excellent tissue boundaries, although slight non-local effects were still present (black arrow). With the excellent boundary information by fast QSM, high quality magnetic susceptibility maps of cerebellar nuclei were obtained using the iLSQR method.

We further applied the iLSQR method to delineate the deep brain nuclei (0.6 mm isotropic resolution, Fig. 8). The susceptibility maps clearly resolved the mammillary bodies (MB), the subthalamic nucleus (STN), the substructures of red nucleus (RN), the lateral dorsal nuclei of thalamus (LDNT), the hippocampus, and inner and outer globus pallidus in excellent detail.

Discussion

In this study, we proposed and developed a general method for estimating streaking artifacts and subtracting them from a given susceptibility map. Specifically, this method used an iterative approach to estimate the streaking artifacts from the ill-conditioned k-space regions using the initial susceptibility estimate by the LSQR method and the susceptibility boundaries estimated using a fast QSM method. By estimating and subtracting out the streaking artifacts, an unbiased quantification of magnetic susceptibility can be achieved with negligible streaking artifacts. The full method, referred to as the iLSQR method, allows for excellent delineation of white matter lesions in MS, and small deep gray matter structures with excellent anatomical detail.

For QSM, one of the most significant sources of error and artifacts is the discrepancy between the theoretical predictions of zero cones in k-space and the non-negligible experimental data at these locations. This discrepancy may suggest the inadequacy of the physical equations in describing the phase contrast of in-vivo biological tissues. There are

many reasons that could contribute to this discrepancy. One reason is that macroscopic magnetic susceptibility of the white matter is anisotropic, and therefore the magnetic response of the brain cannot be adequately described using the isotropic magnetic susceptibility model (Li and Liu, 2013; Li et al., 2012a,b; Liu, 2010; Liu and Li, 2013; Liu et al., 2012a, 2013; Wisnieff et al., 2013; Xie et al., 2014). The second reason is that white matter phase is nonlinearly evolving with TE (Schweser et al., 2011a), which is also dependent on TR and flip angle (Li et al., 2013). The nonlinearly evolving phase is fundamentally related to the microscopic field inhomogeneity induced by the radially aligned myelin lipids (Duyn, 2013; Li et al., 2012a), and the differential T_1, T_2 and T_2^* signal decay among different white matter water compartments. This nonlinearity can be described by advanced physical models considering molecular susceptibility tensors of myelin lipids (Sati et al., 2013; Sukstanskii and Yablonskiy, 2014; Wharton and Bowtell, 2012). This multi-compartment-related effect was not included in the isotropic susceptibility model for QSM. It has been reported that this multi-compartment-related phase offsets could have a significantly larger effect on the QSM than the bulk effects of anisotropic magnetic susceptibility (Wharton and Bowtell, 2014). In addition, the multipole and higher order susceptibility tensors (Liu and Li, 2013) can lead to additional deviations from the physical equation for QSM. The third reason could be the diffusion effects during the 3D volume acquisition, which has been shown to significantly improve the description of the nonlinear phase evolution behavior (Sati et al., 2013). Based on that study, significant water diffusion effects on QSM are expected, but the extent of this effect remains to be defined.

The method proposed here does not address the aforementioned model inadequacy. Rather, the aim is to remove streaking artifacts that may result from this inadequacy and other sources. Particularly, a fast QSM method is used to provide the susceptibility boundaries required for susceptibility artifact estimation. While the magnitude, phase and susceptibility contrast are not necessarily the same (Fig. 7), we used the fast QSM-determined susceptibility to generate the weightings. This method is similar to the threshold-based method by Shumeli et al. (Shmueli et al., 2009), and the superfast dipole inversion (SDI) method of Schweser et al. (Schweser et al., 2013). With the additional repeated k-space averaging, this method gives additional streaking artifacts suppression (Fig. 2). With an additional scaling, this fast QSM method provides a good estimate of magnetic susceptibility with similar susceptibility contrast and the same boundaries. As shown in Fig. 5, this fast QSM method can provide a reasonably accurate estimate of magnetic susceptibility with excellent suppression of streaking artifact and good linearity with iLSQR. As indicated by the arrow in Fig. 5, the difference between fast QSM and iLSQR could be attributed to the inaccurate susceptibility estimation by fast QSM, due to the use of oversimplified phase-susceptibility relationship (Eq. (8)). This fast QSM method works for human brain images, due to the aforementioned discrepancy between the theoretical prediction and the experimental phase data. However, it will not work well for simulated data assuming the isotropic magnetic susceptibility, since the values near the conical surface will be close to zero.

The goal of parameter optimization for iLSQR is to select a set of parameters with effective streaking artifact removal, unbiased susceptibility quantification, and reasonable computation time. As shown in Fig. 3, for the LSQR method, large error tolerance will lead

to underestimated susceptibility and small error tolerance will lead to overestimated magnetic susceptibility, with respect to COSMOS. This is likely due to the aforementioned discrepancy between the applied physical equation and the experimental data, and the increased weighting of the conical regions with more iteration (smaller error tolerances). The error tolerance of ~0.02 gives an unbiased quantification of magnetic susceptibility for LSQR method. This value is consistent with what we used in our previous studies (Argyridis et al., 2014; Li et al., 2014a,b). On the other hand, the susceptibility artifact removal procedure will decrease the slope of the susceptibility contrast with respect to that by COSMOS. Considering these factors, a $D_{2,\,\mathrm{thres}}$ of 0.1 allows for effective removal of streaking artifacts, while its effect in lowering susceptibility contrast is compensated for by selecting an error tolerance of 0.01 for the initial LSQR reconstruction which slightly overestimated susceptibility contrast. With this set of parameters, the iLSQR method provides an unbiased quantification of susceptibility, which is robust over the range of in-plane resolution and slice thickness for routine QSM applications (Fig. 4H). This selection of a D_2 threshold of 0.1 is similar to that used by Schweser et al. (Schweser et al., 2012). The inter-subject reproducibility is demonstrated by the excellent agreement with LSQR using an error tolerance of 0.02 for a group of 10 healthy participants (Fig. 5). Since it is difficult to perform multi-orientation acquisitions routinely, we did not compare iLSQR with COSMOS to further evaluate the inter-subject reproducibility.

COSMOS was used as the reference method since it eliminated the ill-conditioned k-space regions by using multi-orientation acquisition, and it allows for susceptibility reconstruction free of streaking artifacts. Although COSMOS provides the best quality QSM so far, COSMOS-determined susceptibility is not the ground truth, since it is still affected by several factors, e.g. the number and distribution of orientations, imperfect background phase removal, imperfect registration, susceptibility anisotropy, and the aforementioned multi-compartment effects.

The iLSQR method significantly suppressed the streaking artifacts, and allows for a clear delineation of white matter lesions in MS (Fig. 6). From the quantitative comparison (Fig. 6J), the susceptibility contrast by iLSQR is statistically similar to and linearly correlated with that by LSQR, which justifies the use of iLSQR for characterizing the white matter lesions in MS. The trend of larger susceptibility contrast variation of LSQR and the slope of 1.116 between LSQR and iLSQR is possibly related to the larger susceptibility variation within the white matter for the LSQR method. The fast QSM method also provides excellent visualization of white matter susceptibility, and its determined lesion contrast is linearly with iLSQR with a slope of 0.825. The deviation of the slopes from 1 is likely due to the contrast variation across the surrounding white matter as well as and the susceptibility anisotropy and multiple-compartment effects. Future studies are still needed to study the lesion contrast with more accurate physical models and more patients.

The iLSQR method provides excellent delineation of small deep gray matter structures. Fig. 7 shows an excellent delineation of deep cerebellar nuclei by QSM. Deep cerebellar nuclei are among the brain regions that contain the highest amount of iron, mainly in the form of ferritin (Hallgren and Sourander, 1958). Accumulating evidence suggests that the magnetic susceptibility of human brain gray matter mainly originates from its iron concentration, with

a linear relationship of χ(ppm) = 0.89*C (μg/kg) −0.022 (ppm) (Langkammer et al., 2012). According to this relationship, the iron contents in dentate nucleus, fastigial nucleus, globose nucleus, and emboliform nucleus can be estimated as 115 ± 20, 110 ± 13, 103 ± 13, and 117 ± 13 μg/g wet tissue, respectively. These values agree well with previous histological measurement of 103.5 ± 48.6 μg/g in dentate nucleus (Hallgren and Sourander, 1958). Furthermore, the high resolution QSM maps provide excellent delineation of the deep gray matter nuclei in great detail, including inner GP and outer GP, the STN and SN, the mammillary bodies, and the substructures of RN (Fig. 8), which typically can only be imaged using ultra-high field MRI.

To conclude, we developed a general method for estimating streaking artifacts, and combined it with the LSQR method to achieve quantitative susceptibility mapping of the human brain with minimal streaking artifacts. With a fixed set of parameters for the initial QSM reconstruction using LSQR (error tolerance of 0.01) and subsequent streaking artifact removal (D_2 threshold of 0.1), the full method provides an unbiased quantification of tissue susceptibility. The iLSQR method provides improved delineation of the white matter lesions in multiple sclerosis and allows for the high resolution imaging of deep gray matter structures with excellent anatomical detail.

Supplementary Material

Refer to Web version on PubMed Central for supplementary material.

Acknowledgments

This study was supported in part by the National Institutes of Health (NIH) through grants NIBIB P41 EB015897, R21HL122759 and R01 MH096979 and by the National Multiple Sclerosis Society (RG4723) to C.L. W.L. was also supported in part by UL1 TR001119 via the Clinical Translational Science Awards (CTSA).

References

Argyridis I, Li W, Johnson GA, Liu C. Quantitative magnetic susceptibility of the developing mouse brain reveals microstructural changes in the white matter. Neuro Image. 2014; 88:134–142.

de Rochefort L, Liu T, Kressler B, Liu J, Spincemaille P, Lebon V, Wu JL, Wang Y. Quantitative susceptibility map reconstruction from MR phase data using Bayesian regularization: validation and application to brain imaging. Magn Reson Med. 2010; 63:194–206. [PubMed: 19953507]

Deistung A, Schweser F, Wiestler B, Abello M, Roethke M, Sahm F, Wick W, Nagel AM, Heiland S, Schlemmer HP. Quantitative susceptibility mapping differentiates between blood depositions and calcifications in patients with glioblastoma. PLoS ONE. 2013; 8:e57924. [PubMed: 23555565]

Duyn J. MR susceptibility imaging. J Magn Reson. 2013; 229:198–207. [PubMed: 23273840]

Duyn JH, van Gelderen P, Li TQ, de Zwart JA, Koretsky AP, Fukunaga M. High-field MRI of brain cortical substructure based on signal phase. Proc Natl Acad Sci U S A. 2007; 104:11796–11801. [PubMed: 17586684]

Hallgren B, Sourander P. The effect of age on the non-haemin iron in the human brain. J Neurochem. 1958; 3:41–51. [PubMed: 13611557]

He X, Yablonskiy DA. Biophysical mechanisms of phase contrast in gradient echo MRI. Proc Natl Acad Sci U S A. 2009; 106:13558–13563. [PubMed: 19628691]

Koch KM, Papademetris X, Rothman DL, de Graaf RA. Rapid calculations of susceptibility-induced magnetostatic field perturbations for in vivo magnetic resonance. Phys Med Biol. 2006; 51:6381–6402. [PubMed: 17148824]

Kressler B, de Rochefort L, Liu T, Spincemaille P, Jiang Q, Wang Y. Nonlinear regularization for per voxel estimation of magnetic susceptibility distributions from MRI field maps. IEEE Trans Med Imaging. 2010; 29:273–281. [PubMed: 19502123]

Langkammer C, Schweser F, Krebs N, Deistung A, Goessler W, Scheurer E, Sommer K, Reishofer G, Yen K, Fazekas F. Quantitative susceptibility mapping (QSM) as a means to measure brain iron? A post mortem validation study. NeuroImage. 2012; 62:1593–1599. [PubMed: 22634862]

Li W, Liu C. Comparison of magnetic susceptibility tensor and diffusion tensor of the brain. J Neurosci Neuroeng. 2013; 2:431–440. [PubMed: 25401058]

Li W, Wu B, Liu C. Quantitative susceptibility mapping of human brain reflects spatial variation in tissue composition. NeuroImage. 2011; 55:1645–1656. [PubMed: 21224002]

Li W, Wu B, Avram AV, Liu C. Magnetic susceptibility anisotropy of human brain in vivo and its molecular underpinnings. NeuroImage. 2012a; 59:2088–2097. [PubMed: 22036681]

Li X, Vikram DS, Lim IAL, Jones CK, Farrell JAD, van Zijl PCM. Mapping magnetic susceptibility anisotropies of white matter in vivo in the human brain at 7 T. NeuroImage. 2012b; 62:314–330. [PubMed: 22561358]

Li W, Han H, Guidon A, Liu C. Dependence of gradient echo phase contrast on the differential signal decay in subcellular compartments. Proc Int Soc Magn Reson Med. 2013; 21

Li W, Avram AV, Wu B, Xiao X, Liu C. Integrated Laplacian-based phase unwrapping and background phase removal for quantitative susceptibility mapping. NMR Biomed. 2014a; 27:219–227. [PubMed: 24357120]

Li W, Wu B, Batrachenko A, Bancroft-Wu V, Morey RA, Shashi V, Langkammer C, Bellis MDD, Ropele S, Song AW, Liu C. Differential developmental trajectories of magnetic susceptibility in human brain gray and white matter over the lifespan. Hum Brain Mapp. 2014b; 35:2698–2713. [PubMed: 24038837]

Liu C. Susceptibility tensor imaging. Magn Reson Med. 2010; 63:1471–1477. [PubMed: 20512849]

Liu C, Li W. Imaging neural architecture of the brain based on its multipole magnetic response. NeuroImage. 2013; 67:193–202. [PubMed: 23116817]

Liu T, Spincemaille P, de Rochefort L, Kressler B, Wang Y. Calculation of susceptibility through multiple orientation sampling (COSMOS): a method for conditioning the inverse problem from measured magnetic field map to susceptibility source image in MRI. Magn Reson Med. 2009; 61:196–204. [PubMed: 19097205]

Liu C, Li W, Johnson GA, Wu B. High-field (9.4 T) MRI of brain dysmyelination by quantitative mapping of magnetic susceptibility. NeuroImage. 2011a; 56:930–938. [PubMed: 21320606]

Liu T, Liu J, de Rochefort L, Spincemaille P, Khalidov I, Ledoux JR, Wang Y. Morphology enabled dipole inversion (MEDI) from a single-angle acquisition: comparison with COSMOS in human brain imaging. Magn Reson Med. 2011b; 66:777–783. [PubMed: 21465541]

Liu C, Li W, Wu B, Jiang Y, Johnson GA. 3D fiber tractography with susceptibility tensor imaging. NeuroImage. 2012a; 59:1290–1298. [PubMed: 21867759]

Liu T, Surapaneni K, Lou M, Cheng L, Spincemaille P, Wang Y. Cerebral microbleeds: burden assessment by using quantitative susceptibility mapping. Radiology. 2012b; 262:269–278. [PubMed: 22056688]

Liu C, Murphy NE, Li W. Probing white-matter microstructure with higher-order diffusion tensors and susceptibility tensor MRI. Front Integr Neurosci. 2013; 7

Lotfipour AK, Wharton S, Schwarz ST, Gontu V, Schäfer A, Peters AM, Bowtell RW, Auer DP, Gowland PA, Bajaj NP. High resolution magnetic susceptibility mapping of the substantia nigra in Parkinson's disease. J Magn Reson Imaging. 2012; 35:48–55. [PubMed: 21987471]

Marques JP, Bowtell R. Application of a Fourier-based method for rapid calculation of field inhomogeneity due to spatial variation of magnetic susceptibility. Concepts Magn Reson Part B-Magn Reson Eng. 2005; 25B:65–78.

Paige CC, Saunders MA. Lsqr — an algorithm for sparse linear-equations and sparse least-squares. ACM Trans Math Softw. 1982; 8:43–71.

Rauscher A, Sedlacik J, Barth M, Mentzel HJ, Reichenbach JR. Magnetic susceptibility-weighted MR phase imaging of the human brain. Am J Neuroradiol. 2005; 26:736–742. [PubMed: 15814914]

Reichenbach JR. The future of susceptibility contrast for assessment of anatomy and function. NeuroImage. 2012; 62:1311–1315. [PubMed: 22245644]

Salomir R, De Senneville BD, Moonen CTW. A fast calculation method for magnetic field inhomogeneity due to an arbitrary distribution of bulk susceptibility. Concepts in Magnetic Resonance Part B-Magnetic Resonance Engineering. 2003; 19B:26–34.

Sati P, van Gelderen P, Silva AC, Reich DS, Merkle H, de Zwart JA, Duyn JH. Micro-compartment specific T2* relaxation in the brain. NeuroImage. 2013; 77:268–278. [PubMed: 23528924]

Schweser F, Deistung A, Güllmar D, Atterbury M, Lehr B, Sommer K, Reichenbach J. Non-linear evolution of GRE phase as a means to investigate tissue microstructure. Proc Int Soc Magn Reson Med. 2011a; 19

Schweser F, Deistung A, Lehr BW, Reichenbach JR. Quantitative imaging of intrinsic magnetic tissue properties using MRI signal phase: an approach to in vivo brain iron metabolism? NeuroImage. 2011b; 54:2789–2807. [PubMed: 21040794]

Schweser F, Sommer K, Deistung A, Reichenbach JR. Quantitative susceptibility mapping for investigating subtle susceptibility variations in the human brain. NeuroImage. 2012; 62:2083–2100. [PubMed: 22659482]

Schweser F, Deistung A, Sommer K, Reichenbach JR. Toward online reconstruction of quantitative susceptibility maps: superfast dipole inversion. Magn Reson Med. 2013; 69:1581–1593.

Shmueli K, de Zwart JA, van Gelderen P, Li TQ, Dodd SJ, Duyn JH. Magnetic susceptibility mapping of brain tissue in vivo using MRI phase data. Magn Reson Med. 2009; 62:1510–1522. [PubMed: 19859937]

Sukstanskii AL, Yablonskiy DA. On the role of neuronal magnetic susceptibility and structure symmetry on gradient echo MR signal formation. Magn Reson Med. 2014; 71:345–353. [PubMed: 23382087]

Wharton S, Bowtell R. Whole-brain susceptibility mapping at high field: a comparison of multiple- and single-orientation methods. NeuroImage. 2010; 53:515–525. [PubMed: 20615474]

Wharton S, Bowtell R. Fiber orientation-dependent white matter contrast in gradient echo MRI. Proc Natl Acad Sci. 2012; 109:18559–18564. [PubMed: 23091011]

Wharton, S.; Bowtell, R. Effects of white matter microstructure on phase and susceptibility maps. Magn Reson Med. 2014. http://dx.doi.org/10.1002/mrm.25189

Wharton S, Schafer A, Bowtell R. Susceptibility mapping in the human brain using threshold-based k-space division. Magn Reson Med. 2010; 63:1292–1304. [PubMed: 20432300]

Wisnieff C, Liu T, Spincemaille P, Wang S, Zhou D, Wang Y. Magnetic susceptibility anisotropy: cylindrical symmetry from macroscopically ordered anisotropic molecules and accuracy of MRI measurements using few orientations. NeuroImage. 2013; 70:363–376. [PubMed: 23296181]

Wu B, Li W, Guidon A, Liu C. Whole brain susceptibility mapping using compressed sensing. Magn Reson Med. 2012; 67:137–147. [PubMed: 21671269]

Xie, L.; Dibb, R.; Cofer, GP.; Li, W.; Nicholls, PJ.; Johnson, GA.; Liu, C. Susceptibility tensor imaging of the kidney and its microstructural underpinnings. Magn Reson Med. 2014. http://dx.doi.org/10.1002/mrm.25219

Appendix A. Supplementary data

Supplementary data to this article can be found online at http://dx.doi.org/10.1016/j.neuroimage.2014.12.043.

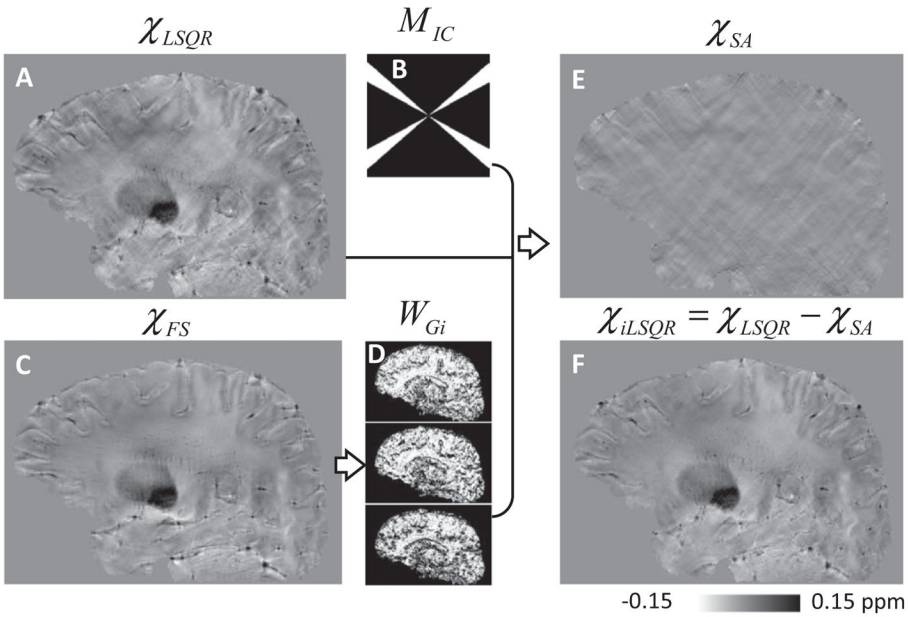

Fig. 1.

Overview of the streaking artifact removal method. A: Initial susceptibility estimate using LSQR. B: The fraction of k-space for streaking artifact estimation. C: The susceptibility map by fast QSM method for estimation of susceptibility boundaries. D: Weights determined using χ_{FS}. E: the estimated susceptibility artifacts. F: The final streaking artifact removed susceptibility map.

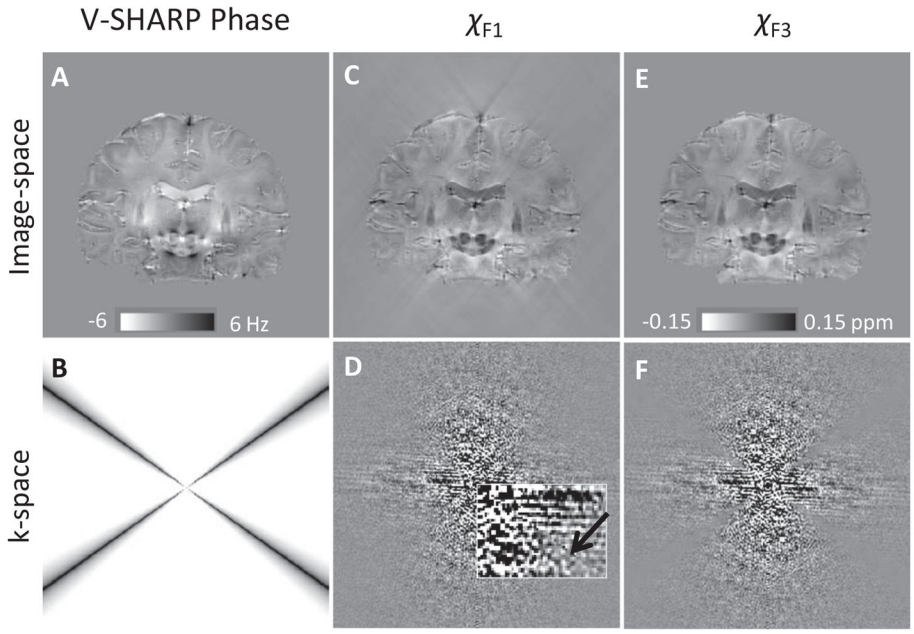

Fig. 2.

Fast QSM method for estimating susceptibility boundaries. A: Tissue phase. B: W_{FS} determined by Eq. (10). C: Susceptibility estimate determined by the first step of Fast QSM method using Eq. (8). D: The k-space corresponding to (C). Arrow pointed to the discontinuities in k-space. E: the final susceptibility estimate using the Eq. (14). F: The k-space corresponding to (E).

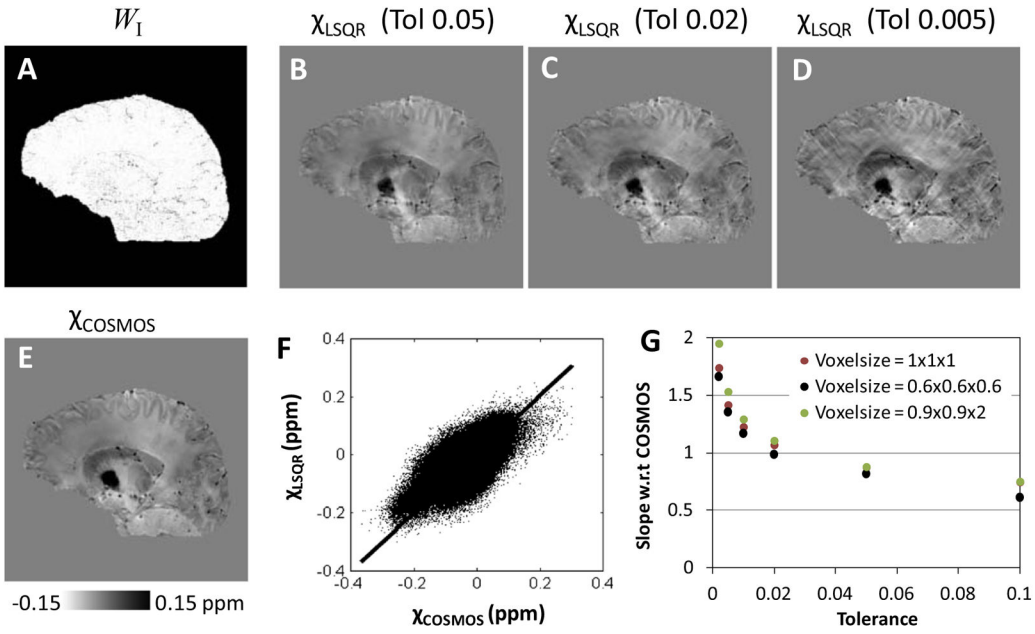

Fig. 3.

Dependence of LSQR-determined susceptibility on the error tolerance. A: The weights for LSQR reconstruction (W_I). B, C and D: LSQR reconstruction using a tolerance of 0.05, 0.02 and 0.005, respectively. E: COSMOS-determined susceptibility. F: Linear regression of QSM by LSQR with a tolerance of 0.02 against that by COSMOS using total least squares (TLS). G: The influence of error tolerance on the slope of TLS linear regression.

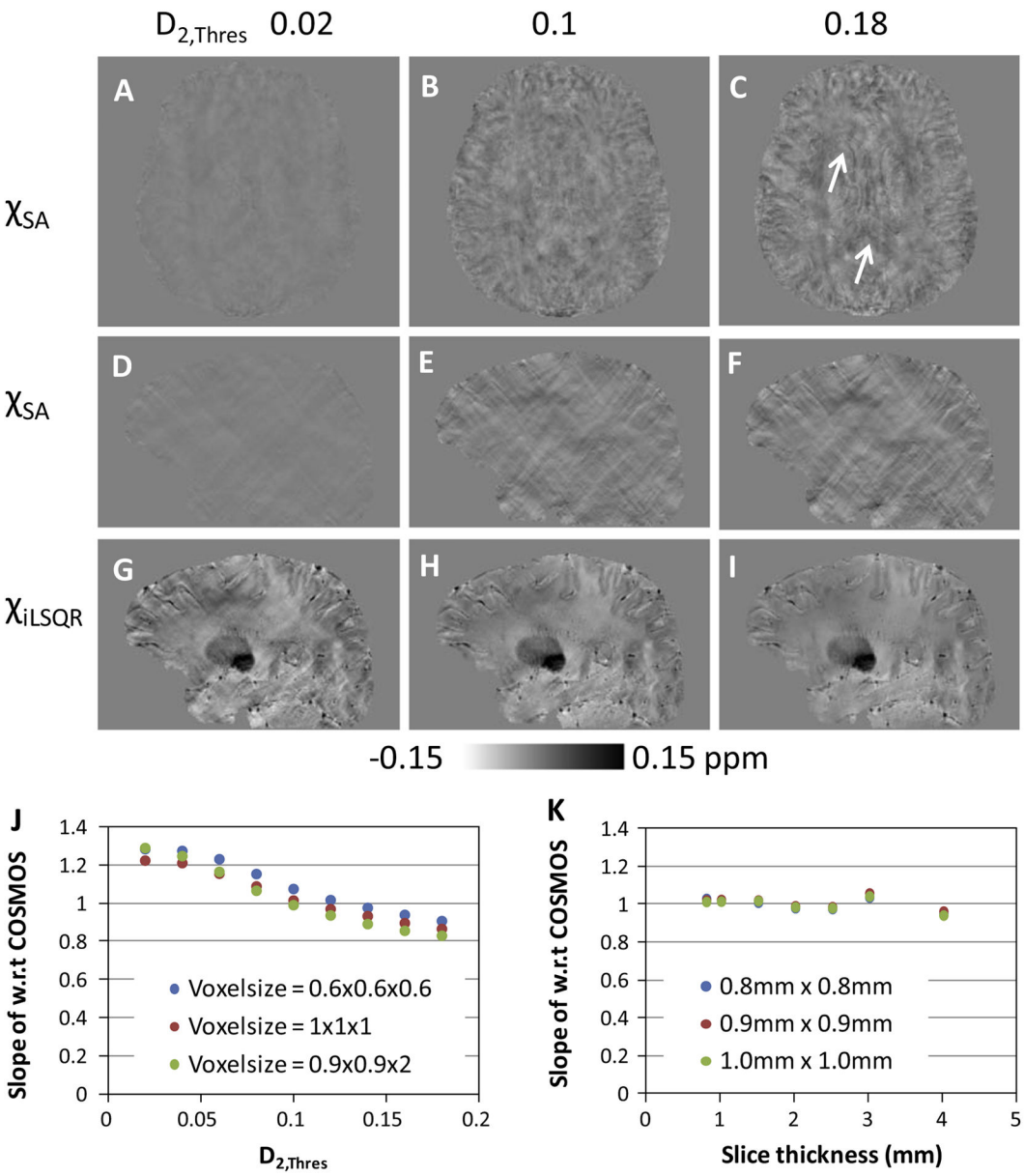

Fig. 4.

Dependence of streaking artifact removal on D_2 threshold. A–F: The susceptibility artifacts estimated using a D_2 threshold of 0.02, 0.1 and 0.18. G–I: The corresponding final susceptibility maps. J: The influence of $D_{2,thres}$ on the slope of TLS linear regression. K: The influence of slice thickness on the slope of TLS linear regression, in which a fixed error tolerance of 0.01 for LSQR and a fixed $D_{2,thres}$ of 0.1 for susceptibility artifact estimation was used.

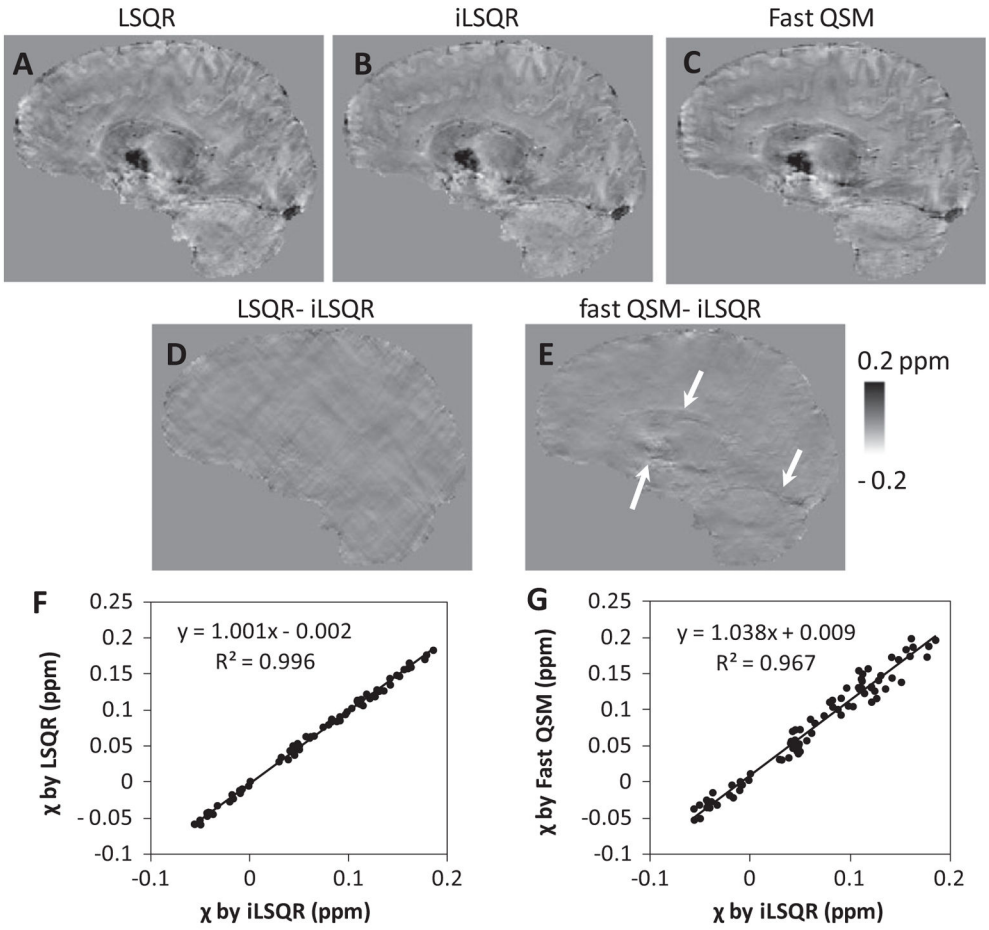

Fig. 5.

The comparison of different QSM methods for a group of 10 subjects with a spatial resolution of 1 × 1 × 1 mm^3. A: Susceptibility using LSQR with an error tolerance of 0.02. B: Susceptibility using iLSQR. C: Susceptibility using fast QSM. D: The susceptibility difference between LSQR and iLSQR. E: The susceptibility difference between fast QSM and iLSQR. F and G: Plot of susceptibility values by LSQR (F) and fast QSM (G) against that by iLSQR in selected ROIs. The ROIs included globus pallidus, putamen, caudate nucleus, red nucleus, substantia nigra, dentate nucleus, splenium of corpus callosum and internal capsule.

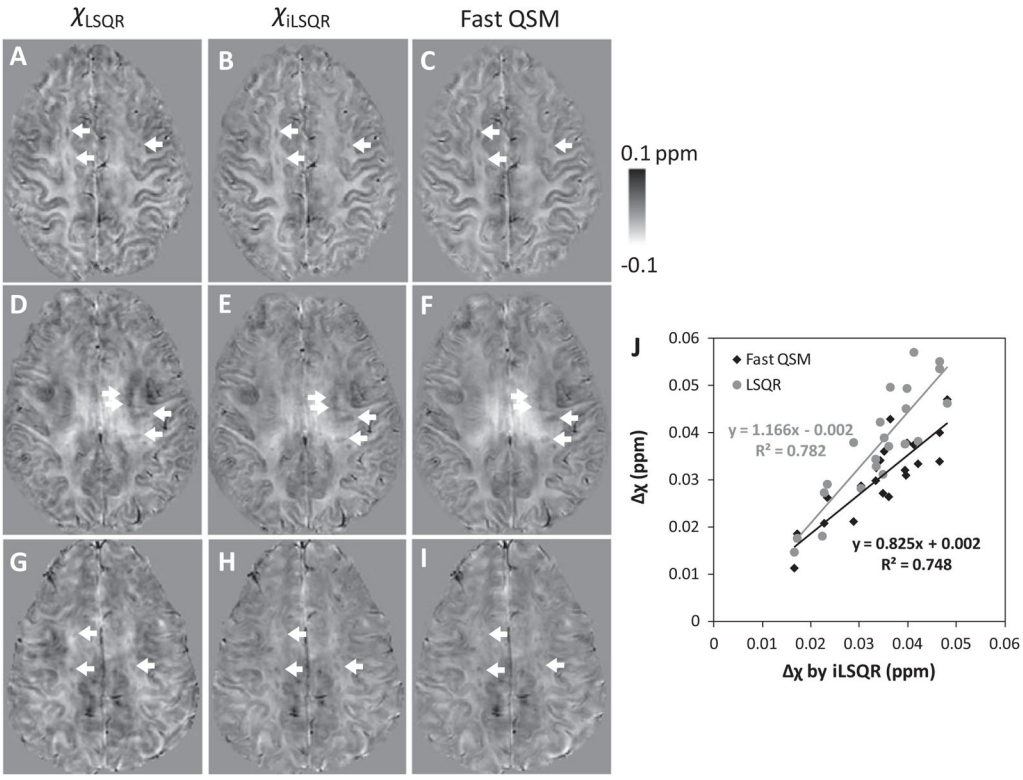

Fig. 6.

Comparison of different QSM methods for delineating MS lesions. A, D and G: Susceptibility map determined using LSQR. B, E and H: Susceptibility map determined using iLSQR. C, F and I: Susceptibility map determined using fast QSM. J: Comparison of susceptibility contrast between white matter lesions and surrounding normal appearing white matter by different QSM methods.

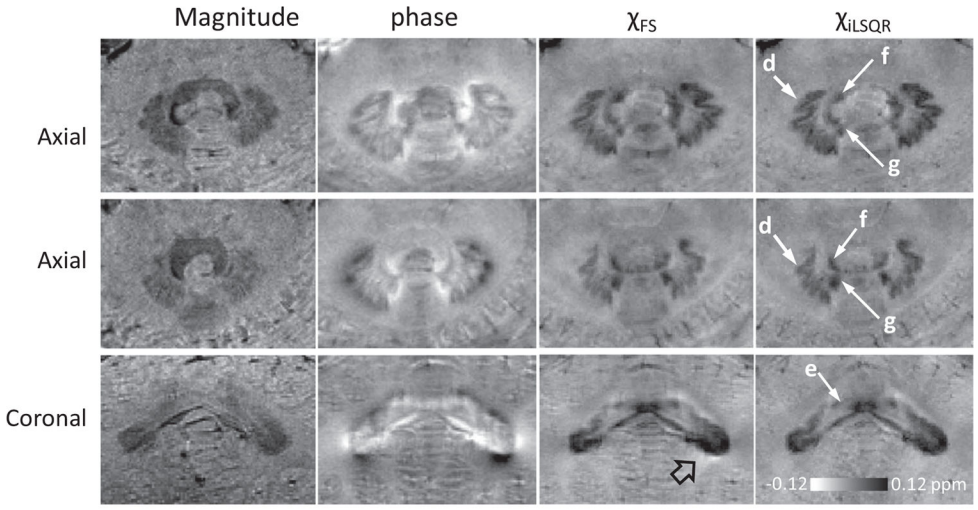

Fig. 7.

Comparison of magnitude, phase, and susceptibility estimates using the fast QSM method, and susceptibility reconstructed using the iLSQR method. d: dentate nucleus; g: globose nucleus; f: fastigial nucleus; e: emboliform nucleus. Magnitude was the summation of the magnitude from all echoes. Hollow black arrow pointed regions with difference between iLSQR and fast QSM method, in which the fast-QSM-determined susceptibility contained more residual non-local effects.

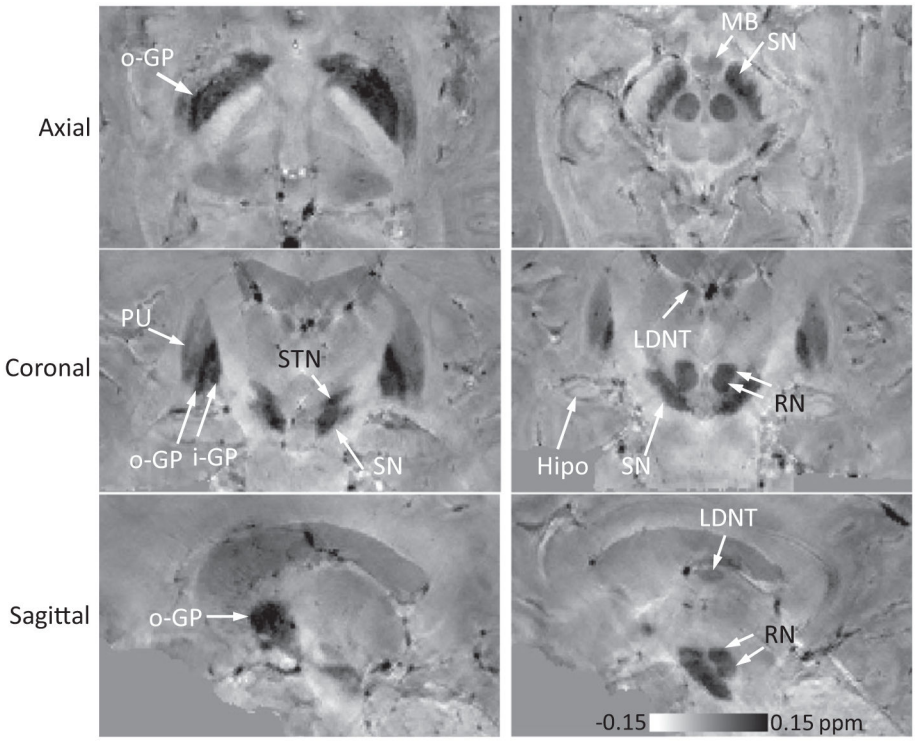

Fig. 8.

High resolution magnetic susceptibility imaging of deep brain gray matter nuclei using the iLSQR method. MB: mammillary bodies; STN: subthalamas nucleus; RN: red nucleus; LDNT: the lateral dorsal nuclei of thalamus; Hipo: hippocampus; the inner and outer globus pallidus (iGP and oGP); SN: substantia nigra; PU: putamen.